Acta Crystallographica Section D
**Biological Crystallography**
ISSN 0907-4449

# Unambiguous determination of H-atom positions: comparing results from neutron and high-resolution X-ray crystallography

**Anna S. Gardberg,[a]* Alexis Rae Del Castillo,[a] Kevin L. Weiss,[a] Flora Meilleur,[a,b] Matthew P. Blakeley[c] and Dean A. A. Myles[a]**

[a]Oak Ridge National Laboratory, USA, [b]North Carolina State University, USA, and [c]Institut Laue–Langevin, France

Correspondence e-mail: anna.s.gardberg@gmail.com

Received 7 December 2009
Accepted 9 February 2010

**PDB References:** rubredoxin, 3kyu; 3kyv; 3kyw; 3kyx; 3kyy.

The locations of H atoms in biological structures can be difficult to determine using X-ray diffraction methods. Neutron diffraction offers a relatively greater scattering magnitude from H and D atoms. Here, 1.65 Å resolution neutron diffraction studies of fully perdeuterated and selectively $CH_3$-protonated perdeuterated crystals of *Pyrococcus furiosus* rubredoxin (D-rubredoxin and HD-rubredoxin, respectively) at room temperature (RT) are described, as well as 1.1 Å resolution X-ray diffraction studies of the same protein at both RT and 100 K. The two techniques are quantitatively compared in terms of their power to directly provide atomic positions for D atoms and analyze the role played by atomic thermal motion by computing the $\sigma$ level at the D-atom coordinate in simulated-annealing composite D-OMIT maps. It is shown that 1.65 Å resolution RT neutron data for perdeuterated rubredoxin are ~8 times more likely overall to provide high-confidence positions for D atoms than 1.1 Å resolution X-ray data at 100 K or RT. At or above the 1.0$\sigma$ level, the joint X-ray/neutron (XN) structures define 342/378 (90%) and 291/365 (80%) of the D-atom positions for D-rubredoxin and HD-rubredoxin, respectively. The X-ray-only 1.1 Å resolution 100 K structures determine only 19/388 (5%) and 8/388 (2%) of the D-atom positions above the 1.0$\sigma$ level for D-rubredoxin and HD-rubredoxin, respectively. Furthermore, the improved model obtained from joint XN refinement yielded improved electron-density maps, permitting the location of more D atoms than electron-density maps from models refined against X-ray data only.

## 1. Introduction

About half of the atoms in any protein molecule are typically hydrogen. The geometric positions of the majority of these H atoms can be predicted chemically from the positions of their C, N or O binding partners. However, when protein function and biochemical reactions involve the transfer of H atoms it is important to determine these positions experimentally. Likewise, it is sometimes important to know the protonation states of amino-acid side chains, water molecules and ligands, particularly those at enzyme active sites.

Crystallographic structural information for proteins is normally obtained by X-ray diffraction. The X-ray diffraction signal is proportional to the atomic number $Z$, so hydrogen with its lone electron scatters X-rays only poorly. Increasing the X-ray dose tends to damage protein crystals, even when the data are collected at 100 K (Garman & Nave, 2009), so

that the signal cannot easily be enhanced by increasing the X-ray intensity. Crystals of extremely high quality diffracting to unusually high resolution do permit the observation of some fraction of the H atoms for a small number of proteins (Rosenbaum *et al.*, 2006; Dauter *et al.*, 1997; Esposito *et al.*, 2002; Petrova & Podjarny, 2004; Schmidt & Lamzin, 2002). In the 0.75 Å resolution structure of hydrophobin, for instance, 59.7% of the H atoms were observed above the zero level of density in an OMIT map (Hakanpää *et al.*, 2006). However, the 0.85 Å resolution structure of TEM-1 $\beta$-lactamase revealed the positions of 70% of its H atoms above the 1.5$\sigma$ level in hydrogen-OMIT $F_o - F_c$ maps (Minasov *et al.*, 2002), indicating that resolution alone is not sufficient for the confident placement of H atoms. Indeed, in the context of locating H atoms in small-molecule structures, it was noted in 1965 that

> the ratio of the peak height of an atom to the standard deviation of the electron density (signal-to-noise ratio) must go through a maximum as a function of scattering angle

(Laplaca & Ibers, 1965). So, while the 0.95 Å resolution $F_o - F_c$ difference maps for *Pyrococcus furiosus* rubredoxin showed electron density ($\sigma$ level not given) for ∼50% of H-atom positions (Bau *et al.*, 1998), it was reported that the maps from the 1.1 Å resolution structure of the protein were actually cleaner. Thus, ultrahigh-resolution X-ray data are not necessarily sufficient to obtain direct information on H-atom locations.

Another diffraction technique that enables H-atom (used here to mean protium or deuterium) positions to be determined is neutron crystallography (Blakeley, 2009). Neutrons interact directly with the atomic nucleus and neutron diffraction scattering power does not depend on the atomic number $Z$; indeed, different isotopes of the same element can have different scattering lengths. D atoms scatter neutrons with a magnitude similar to C, O and N atoms. $^1$H atoms scatter with a smaller magnitude and opposite sign. In practice, D-atom positions can readily be located in neutron structures even at relatively low resolution (2.2 Å; Hazemann *et al.*, 2005; Blum *et al.*, 2009). Furthermore, neutron diffraction does not result in detectable radiation damage to protein crystal samples (Kossiakoff, 1983), so data collection can proceed under ambient conditions without the risks of cryoprotection (increased strain and mosaicity).

The technique of neutron crystallography is not without technical limitations: crystals 1000-fold larger than those typically used in X-ray crystallography are required to offset the weak flux of neutron sources and several days or weeks are generally required for data collection. This requirement for large crystal volumes can be alleviated around tenfold by full perdeuteration of the protein during expression followed by crystal growth in deuterated buffers (Shu *et al.*, 2000; Meilleur *et al.*, 2004; Hazemann *et al.*, 2005; Budayova-Spano *et al.*, 2006).

Previous work with perdeuterated crystals has shown that perdeuteration does not significantly alter the overall three-dimensional structure of the protein (Gamble *et al.*, 1994; Di Costanzo *et al.*, 2007; Meilleur *et al.*, 2005). As observed in endothiapepsin, this also applies to partial exchange of H atoms with D atoms by soaking (Coates *et al.*, 2001). However, the overall increase in hydrophobicity can cause shifts in the optimum crystallization condition, which in turn can lead to changes in configurations at pH-dependent sites (Liu *et al.*, 2007). Full perdeuteration increases the signal-to-noise ratio for neutron protein crystallography in two ways: the coherent scattering magnitude of deuterium is approximately twofold greater than that of protium hydrogen and its incoherent scattering background is 40-fold less (Sears, 1992; Gamble *et al.*, 1994). These phenomena result in an approximately tenfold improvement in the signal-to-noise ratio of the data, enabling the use of smaller crystals and/or larger unit cells. Further, the nuclear density maps are considerably improved owing to elimination of the cancellation phenomenon, which occurs when a $^1$H atom (which has a negative neutron scattering length) is bound to an atom with a positive scattering length, resulting in an apparent nuclear density of zero along the chemical bond at medium (∼2 Å) resolution; this effect is less problematic in small-molecule neutron studies, for which data can be obtained to better than 1.2 Å resolution.

Here, we describe 1.65 Å resolution neutron diffraction studies of fully perdeuterated and selectively $CH_3$-protonated perdeuterated crystals of *P. furiosus* rubredoxin (D-rubredoxin and HD-rubredoxin, respectively) at room temperature (RT) as well as 1.1 Å resolution X-ray diffraction studies of the same protein at both RT and 100 K. We quantitatively compare these two techniques in terms of their power to directly provide atomic positions for H atoms and analyze the role played by atomic thermal motion by computing the $\sigma$ level at the H-atom coordinate in simulated-annealing composite H-select OMIT maps. We show that 1.65 Å resolution RT neutron data for perdeuterated rubredoxin are ∼8 times more powerful for determining high-confidence positions for D atoms than 1.1 Å resolution X-ray data at 100 K or RT.

## 2. Materials and methods

### 2.1. *P. furiosus* rubredoxin

*P. furiosus* is an anaerobic sulfur-reducing species of Archaea. It exhibits optimum growth near 373 K. *P. furiosus* rubredoxin (PrRd) is a 53-amino-acid protein (molecular weight 5.8 kDa) containing an Fe atom bound to the S atoms of four cysteine residues in a nearly regular tetrahedron. Rubredoxins are involved in electron transfer (Lovenberg & Sobel, 1965). PfRd has a long history as a crystallographic test system and is of interest for its remarkable high-temperature stability.

### 2.2. Expression and purification of perdeuterated rubredoxin from *P. furiosus*

A pET24d expression vector harboring the PfRd gene, a gift from Michael Adams and Frank Jenney at the University of Georgia, was transformed into *Escherichia coli* strain BL21 (DE3) and plated on LB agar containing kanamycin (50 µg ml$^{-1}$). Minimal medium with kanamycin selection

**Table 1**
X-ray data-collection and processing statistics.

Values in parentheses are for the highest resolution shell.

| | D-rubredoxin | D-rubredoxin | HD-rubredoxin | HD-rubredoxin |
|---|---|---|---|---|
| Temperature (K) | 295 | 100 | 295 | 100 |
| Detector limit (Å) | 1.6 | 1.1 (no offset) | 1.1 (no offset) | 1.1 (no offset) |
| Wavelength (Å) | 1.54 | 1.0 | 1.0 | 1.0 |
| Data resolution range(s) (Å) | 12.8–1.6 | 43.23–2.0, 27.04–1.1 | 27.5–1.1 | 43.07–2.0, 26.88–1.1 |
| Detector distance (mm) | 75 | 200, 85 | 85 | 200, 85 |
| Frame width (°) | 1.5 | 1, 0.5 | 1 | 1, 0.5 |
| Exposure time (s) | 300 | 0.15, 0.5 | 0.5 | 0.2, 0.5 |
| Exposure time (s deg$^{-1}$) | | 0.15, 1.0 | 0.5 | 0.2, 1.0 |
| Frames | 98 | 150, 300 | 99 | 300, 110 |
| $R_{\rm merge}$† | 0.067 (0.128) | 0.095 (0.089) | 0.12 (0.4) | 0.103 (0.13) |
| $R_{\rm p.i.m.}$ (all $I^+$ and $I^-$)‡ | 0.031 (0.057) | 0.043 (0.053) | 0.075 (0.278) | 0.044 (0.071) |
| Unique reflections | 6833 (968) | 21178 (2935) | 21725 (3063) | 20908 (2930) |
| Mean $I/\sigma(I)$ | 18.8 (11.9) | 17.4 (13.7) | 8.9 (2.3) | 14 (9.7) |
| Completeness (%) | 91.9 (90.4) | 99.4 (96.5) | 98.8 (97.3) | 99.5 (97.4) |
| Multiplicity | 5.7 (5.9) | 5.6 (4.2) | 3.7 (3.2) | 6.2 (4.9) |

† $R_{\rm merge} = \sum_{hkl}\sum_i |I_i(hkl) - \langle I(hkl)\rangle| / \sum_{hkl}\sum_i I_i(hkl)$, where $I(hkl)$ is the intensity of reflection $hkl$, $\sum_{hkl}$ is the sum over all reflections and $\sum_i$ is the sum over $i$ measurements of reflection $hkl$. ‡ $R_{\rm p.i.m.} = \sum_{hkl}[1/(N-1)]^{1/2}\sum_i |I_i(hkl) - \langle I(hkl)\rangle| / \sum_{hkl}\sum_i I_i(hkl)$ (Weiss, 2001), where $I(hkl)$ is the intensity of reflection $hkl$, $\sum_{hkl}$ is the sum over all reflections and $\sum_i$ is the sum over $i$ measurements of reflection $hkl$.

(50 µg ml$^{-1}$) was utilized in all subsequent cultures. With the exception of doubling the $FeCl_3$ concentration and utilizing a $ZnSO_4$-free solution of trace metals, the minimal medium was prepared as described previously (Meilleur *et al.*, 2004). $ZnSO_4$ was excluded in order to avoid expression of the zinc-substituted form of rubredoxin (Eidsness *et al.*, 1997; Jenney & Adams, 2001). When necessary, salts containing exchangeable H atoms were replaced with deuterium by two $D_2O$ dissolution–evaporation cycles utilizing a rotary evaporator. Prior to expression of perdeuterated rubredoxin, single colonies were cultivated on hydrogenated minimal media agar and transferred to deuterated minimal media agar. After growth on deuterated agar, liquid deuterated minimal medium was inoculated and cultured. Following three cycles of $D_2O$ adaptation, 1 l cultures were inoculated at a 1:20 dilution and grown at 310 K. When the cultures reached an $OD_{600}$ of 0.9, the temperature was lowered to 303 K and protein expression was induced with 0.5 m*M* IPTG. After 10 h induction, the cells were pelleted, flash-frozen in liquid nitrogen and stored at 193 K. The purification of PfRd has been described in detail elsewhere (Jenney & Adams, 2001) and perdeuterated PfRd was purified in a similar manner using a combination of heat treatment, anion-exchange chromatography (HiTrap Q HP column; GE Healthcare) and gel filtration (HiLoad 16/60 Superdex 75; GE Healthcare). The three N-terminal forms of the protein were not separated. During the purification, the PfRd-containing fractions were characterized by their UV–visible absorption spectra and their concentrations were determined from the absorbance at 494 nm ($\varepsilon_{494\,\rm nm}$ = 9.22 m$M^{-1}$ cm$^{-1}$). Following gel filtration, fractions with an absorbance ratio ($A_{494\,\rm nm}/A_{280\,\rm nm}$) of greater than 0.35 were pooled and concentrated to 40 mg ml$^{-1}$. Prior to crystallization, three dilution–concentration cycles using a 1:10 dilution into 99% $D_2O$ were performed in a centrifugal concentrator to remove the hydrogenated gel-filtration buffer.

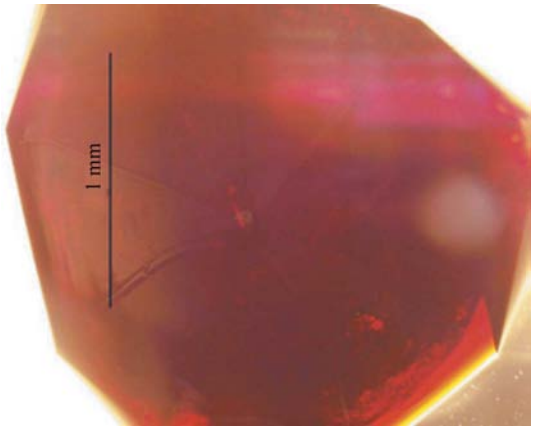


**Figure 1**
The crystal of HD-rubredoxin used for neutron diffraction data collection.

The expression and purification of $CH_3$-protonated deuterated *P. furiosus* rubredoxin (HD-rubredoxin) has been described elsewhere (Weiss *et al.*, 2008).

### 2.3. Crystallization

The crystallization of HD-rubredoxin from $D_2O$-based phosphate buffer has been described elsewhere (Weiss *et al.*, 2008). A crystal of HD-rubredoxin is shown in Fig. 1. The crystallization of D-rubredoxin followed the same protocol.

### 2.4. X-ray data collection and processing

**2.4.1. 100 K synchrotron X-ray data collection for $CH_3$-protonated deuterated rubredoxin (HD-rubredoxin).** A crystal of ∼0.5 mm edge length was mounted on a pin in a loop. After cryoprotection with mother liquor containing 25% glycerol, the crystal was flash-cooled in liquid nitrogen and transferred to the goniometer. Data collection consisted of two passes. For the high-resolution pass the crystal-to-detector distance was 85 mm. 300 frames of width 0.5°, each with a 0.5 s duration, were obtained using a MAR225 detector on the SER-CAT 22BM-D beamline at the APS. For the low-resolution pass to correctly measure overloaded spots, a crystal-to-detector distance of 200 mm was employed and 110 frames were obtained with 0.2 s exposure time each. The frame width was 1°. Data were processed with the *Elves* (Holton & Alber, 2004) interface to *MOSFLM* (Leslie *et al.*, 1986) and *SCALA* (Evans, 1997). Data-collection and processing statistics are presented in Table 1.

**2.4.2. Room-temperature synchrotron X-ray data collection for HD-rubredoxin.** A crystallization drop of HD-rubredoxin was prepared identically to that used for neutron

**Table 2**
Neutron data-collection and processing statistics.

| | D-rubredoxin | HD-rubredoxin |
|---|---|---|
| Temperature (K) | 295 | 295 |
| Wavelength (range in Å) | 3.3–4.2 | 3.1–4.2 |
| Data resolution range (Å) | 27.12–1.68 | 27.2–1.65 |
| Crystal-to-detector distance (mm) | 200 (fixed) | 200 (fixed) |
| Frame width | Stationary | Stationary |
| Setting spacing (°) | 5, 7 | 5 |
| Exposure time (h) | 4 | 4 |
| Frames | 29 | 20 |
| $R_{\rm merge}$† | 0.095 (0.099) | 0.092 (0.108) |
| $R_{\rm p.i.m.}$ (all $I^+$ and $I^-$)‡ | 0.04 (0.086) | 0.035 (0.074) |
| Total No. of unique reflections | 5311 (304) | 4602 (302) |
| Mean $I/\sigma(I)$ | 14.9 (4.1) | 16.0 (5.2) |
| Completeness (%) | 82.3 (34) | 71.6 (33.6) |
| Multiplicity | 6.1 (1.4) | 5.9 (1.9) |

† $R_{\rm merge} = \sum_{hkl}\sum_i |I_i(hkl) - \langle I(hkl)\rangle| / \sum_{hkl}\sum_i I_i(hkl)$, where $I(hkl)$ is the intensity of reflection $hkl$, $\sum_{hkl}$ is the sum over all reflections and $\sum_i$ is the sum over $i$ measurements of reflection $hkl$. ‡ $R_{\rm p.i.m.} = \sum_{hkl}[1/(N-1)]^{1/2}\sum_i |I_i(hkl) - \langle I(hkl)\rangle| / \sum_{hkl}\sum_i I_i(hkl)$ (Weiss, 2001), where $I(hkl)$ is the intensity of reflection $hkl$, $\sum_{hkl}$ is the sum over all reflections and $\sum_i$ is the sum over $i$ measurements of reflection $hkl$.

data collection. A crystal of ∼0.5 mm edge length was mounted in a Mylar loop on a pin and protected from solvent loss by a plug of mother liquor in a MiTeGen MicroRT thin-walled polymer mount. 100° of data were collected on the SER-CAT 22BM-D beamline at the APS. Each frame consisted of a 1° oscillation with 0.5 s exposure time. To counter the heating effect of the X-ray beam, the beam was attenuated to 25% of full strength and a 295 K gas stream was flowed over the crystal. Diffraction data were collected at λ = 1.00 Å using a MAR225 detector at a crystal-to-distance of 85 mm. Data were integrated and scaled with the *Elves* (Holton & Alber, 2004) interface to *MOSFLM* (Leslie *et al.*, 1986) and *SCALA* (Evans, 1997). Data-collection and processing statistics are presented in Table 1.

**2.4.3. 100 K synchrotron X-ray data collection for fully perdeuterated rubredoxin (D-rubredoxin)**. A crystal of ∼0.5 mm edge length was mounted on a pin in a loop. After cryoprotection with mother liquor containing 25% glycerol, the crystal was flash-cooled in liquid nitrogen and transferred to the goniometer. Data collection consisted of two passes. For the high-resolution pass the crystal-to-detector distance was 85 mm. 300 frames of width 0.5°, each with a 0.5 s duration, were obtained using a MAR225 detector on the SER-CAT 22BM-D beamline at the APS. For the low-resolution pass, a crystal-to-detector distance of 200 mm was employed and 110 frames with 0.15 s exposure time each were obtained. The frame width was 1°. Data were integrated and scaled with the *Elves* (Holton & Alber, 2004) interface to *MOSFLM* (Leslie *et al.*, 1986) and *SCALA* (Evans, 1997). Data-collection and processing statistics are presented in Table 1.

**2.4.4. Room-temperature in-house X-ray data collection for D-rubredoxin**. A ∼0.75 × 2 × 2 mm crystal of D-rubredoxin was mounted in a 3 mm diameter quartz capillary. 147° of data were collected on a MAR345 detector on a home source at North Carolina State University (NCSU). Each frame consisted of a 1.5° oscillation with 5 min exposure. Data were integrated and scaled with *MOSFLM* (Leslie *et al.*, 1986) and *SCALA* (Evans, 1997). Data-collection and processing statistics are presented in Table 1. These data were used for joint X-ray/neutron (XN) structure refinement.

### 2.5. Neutron data collection and processing

The data-collection and processing procedures for the ∼4.1 mm$^3$ crystal of HD-rubredoxin have been described elsewhere (Weiss *et al.*, 2008). For D-rubredoxin, a crystal with dimensions of 2 × 1.5 × 1.3 mm (∼3.9 mm$^3$) was mounted in a 3 mm diameter quartz capillary. Crystal hydration was maintained with reservoirs of sodium/potassium phosphate solution that were placed at both capillary ends. Wax was used for sealing. Neutron quasi-Laue data were collected at 293 K on the LADI-III detector installed on end-station T17 of cold neutron guide H142 at ILL. The data were collected in three passes. The first pass consisted of ten images collected in stationary exposures of 4 h each with a $\varphi$-step separation of 10° between images. The crystal was not reoriented for the second pass, which also consisted of ten images of 4 h each with a $\varphi$-step separation of 10° between images but at a 5° offset from the first set. The crystal was reoriented for the third pass, which consisted of 12 images of 4 h exposure each with a $\varphi$-step separation of 7° between images. A typical quasi-Laue neutron diffraction pattern is shown in Fig. 2.

The neutron Laue data were processed using the Daresbury Laboratory software *LAUEGEN* modified to account for the cylindrical geometry of the detector (Campbell *et al.*, 1998). *LSCALE* (Arzt *et al.*, 1999) was used to derive the wavelength-normalization curve using the recorded intensities of symmetry-equivalent reflections measured at different wavelengths as well as to perform initial image-by-image scaling. The data were fully scaled and merged using *SCALA* (Evans, 1997). Neutron data-collection and reduction statistics are summarized in Table 2. The reflections in the last resolution shell (1.74–1.65 Å) were strong [mean $I/\sigma(I)$ = 5.2] and were therefore included despite the

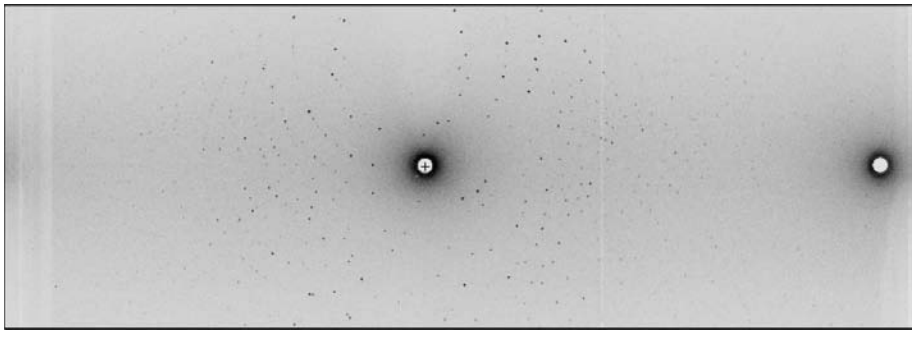

**Figure 2**
Neutron diffraction pattern from a crystal of D-rubredoxin collected on the LADI-III instrument at the ILL. The sweeping arcs are typical of a Laue (polychromatic) diffraction image.

**Table 3**
X-ray refinement statistics.

| | D-rubredoxin | D-rubredoxin | HD-rubredoxin | HD-rubredoxin | HD-rubredoxin |
|---|---|---|---|---|---|
| Temperature (K) | 100 | 295 | 295 | 295 | 100 |
| X-ray or neutron | X-ray | X-ray joint | X-ray joint | X-ray alone | X-ray |
| Resolution (Å) | 1.1 | 1.6 | 1.1 | 1.1 | 1.1 |
| Program | *REFMAC*5 | *phenix.refine* | *phenix.refine* | *REFMAC*5 | *REFMAC*5 |
| Waters | 138 | 28 | 37 | 63 | 108 |
| $R_{work}$† | 0.106 | 0.169 | 0.145 | 0.152 | 0.128 |
| $R_{free}$† | 0.125 | 0.197 | 0.156 | 0.165 | 0.147 |
| R.m.s.d. | | | | | |
| Bonds (Å) | 0.015 | 0.005 | 0.014 | 0.014 | 0.024 |
| Bond angles | 1.612 | 0.969 | 1.426 | 1.508 | 1.951 |
| PDB code | 3kyu | 3kyx | 3kyy | 3kyw | 3kyv |

† $R = \sum_{hkl} ||F_{obs}| - |F_{calc}|| / \sum_{hkl} |F_{obs}|$, where $F_{obs}$ and $F_{calc}$ are the observed and calculated structure factors, respectively. For $R_{free}$ the sum is performed on the test-set reflections (~5% of the total reflections) and for $R_{work}$ on the remaining reflections.

**Table 4**
Neutron refinement statistics.

| | D-rubredoxin | HD-rubredoxin |
|---|---|---|
| Temperature (K) | 295 | 295 |
| Refinement note | Neutron (joint with 1.6 Å X-ray data) | Neutron (joint with 1.1 Å X-ray data) |
| Resolution (Å) | 1.675 | 1.662 |
| Program | *phenix.refine* | *phenix.refine* |
| Refinement | | |
| No. of non-HD atoms | 446 | 468 |
| Protein | 418 | 431 |
| Waters | 28 | 37 |
| $R_{work}$† | 0.248 | 0.187 |
| $R_{free}$† | 0.267 | 0.202 |
| PDB code | 3kyx | 3kyy |

† $R = \sum_{hkl} ||F_{obs}| - |F_{calc}|| / \sum_{hkl} |F_{obs}|$, where $F_{obs}$ and $F_{calc}$ are the observed and calculated structure factors, respectively. For $R_{free}$ the sum is performed on the test-set reflections (~5% of the total reflections) and for $R_{work}$ on the remaining reflections.

relatively low completeness in the shell. The last shell for which data completeness exceeded 50% was 1.82–1.78 Å.

### 2.6. Structure solution and refinement

**2.6.1. X-ray structure solution and refinement**. The 100 K X-ray structure of HD-rubredoxin was solved by SAD using automated *SHELX* (Sheldrick, 2008) procedures in the *CCP*4*i* interface (Collaborative Computational Project, Number 4, 1994). Despite the fact the anomalous signal ($f''$) for Fe is only 1.5 $e^-$ at $\lambda$ = 1.00 Å, the initial maps were clear enough to build 51 of the 54 protein residues. After one cycle of refinement in *REFMAC*5 (Murshudov *et al.*, 1997), the remaining protein residues and 60 water molecules were built. The final number of water molecules for this structure was 108, compared with the 137 located in the 0.95 Å resolution refined rubredoxin structure 1brf (Bau *et al.*, 1998). For the solution of the other X-ray structures, the 0.95 Å resolution 1brf structure (Bau *et al.*, 1998) was stripped of water molecules and used as a starting model for molecular replacement in *MOLREP* (Vagin & Teplyakov, 1997) or direct rigid-body fits with *REFMAC*5 (Murshudov *et al.*, 1997).

The 100 K 1.1 Å resolution structures were refined with *REFMAC*5 iterated with rebuilding in *Coot* (Emsley & Cowtan, 2004). Many atoms were modelled with anisotropic thermal displacement parameters. After several cycles of rebuilding and refinement, the agreement indices converged to $R_{work}$ = 10.6%, $R_{free}$ = 12.5% for fully perdeuterated rubredoxin and $R_{work}$ = 12.8%, $R_{free}$ = 14.7% for $CH_3$-protonated perdeuterated rubredoxin. The RT 1.1 Å resolution HD-rubredoxin X-ray structure was refined in two ways: on its own with *REFMAC*5 ($R_{work}$ = 15.2%, $R_{free}$ = 16.5%) and as part of a joint XN refinement with the neutron data from the same crystal, as discussed below. The positions of the D atoms in all of the X-ray-only refinements were refined in 'riding' mode. The RT 1.6 Å resolution D-rubredoxin X-ray structure was refined in joint XN mode as described below. Final refinement statistics are presented in Table 3. The computed r.m.s.d. for all non-H protein atoms in the refined 100 K X-ray structures of HD-rubredoxin (SAD) and 1brf was very small at only 0.125 Å, indicating that perdeuteration does not significantly change the structure of PfRd. The computed r.m.s.d. for all non-H protein atoms in the refined 100 K X-ray structures of HD-rubredoxin and D-rubredoxin (molecular replacement from 1brf) was even smaller at only 0.075 Å.

**2.6.2. Neutron structure solution and joint XN refinement**. A solvent-less rigid-body-refined RT X-ray structure was used as the starting model. D atoms were substituted for all H atoms (or all except valine and leucine methyl groups in the case of HD-rubredoxin) with the Linux utility *sed* or *phenix.ready_set*. Refinement was performed with *phenix.refine* (Adams *et al.*, 2002) in joint X-ray–neutron mode. In the joint XN refinements, D-atom positions and ADPs were refined individually. Neutron refinement statistics are presented in Table 4.

For D-rubredoxin, the initial refinement results for the neutron data were $R_{work}$ = 35.2%, $R_{free}$ = 35.9%. After four cycles of rebuilding in *Coot* and refinement with *phenix.refine*, these statistics were $R_{work}$ = 24.8%, $R_{free}$ = 26.7%. All of the atoms were refined isotropically. The O atoms of water molecules were positioned from either electron density or nuclear density. 38 D atoms of water molecules were explicitly assigned when nuclear $F_o - F_c$ map density made their positions clear. Of the 28 heavy-water molecules refined in this structure, 13 were ultimately assigned as full $D_2O$ molecules with 'boomerang' nuclear density (Ostermann *et al.*, 2002), a further ten had 'stick' density for the O and one D atom and the remaining five water molecules displayed only spherical nuclear density. In comparison, in the 1.5 Å neutron structure reported for H/D-exchanged rubredoxin (Kurihara *et al.*, 2004) 37 hydration waters were modelled, of which 15 had all three atoms fully located.

For HD-rubredoxin joint XN refinement, the initial model fit parameters to the neutron data were $R_{work}$ = 27.9%, $R_{free}$ = 26.1%; after seven cycles of rebuilding in *Coot* and refinement with *phenix.refine* these statistics were

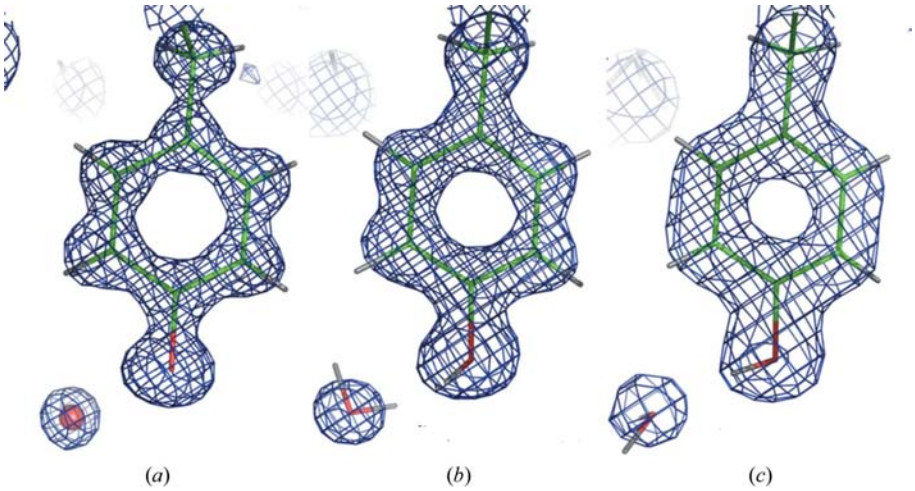


**Figure 3**
X-ray electron-density maps. Simulated-annealing composite D-OMIT electron density at 1.5$\sigma$ computed from X-ray data sets from HD-rubredoxin. (*a*) 100 K, X-ray only. (*b*) 295 K, X-ray only. (*c*) 295 K, joint XN refinement

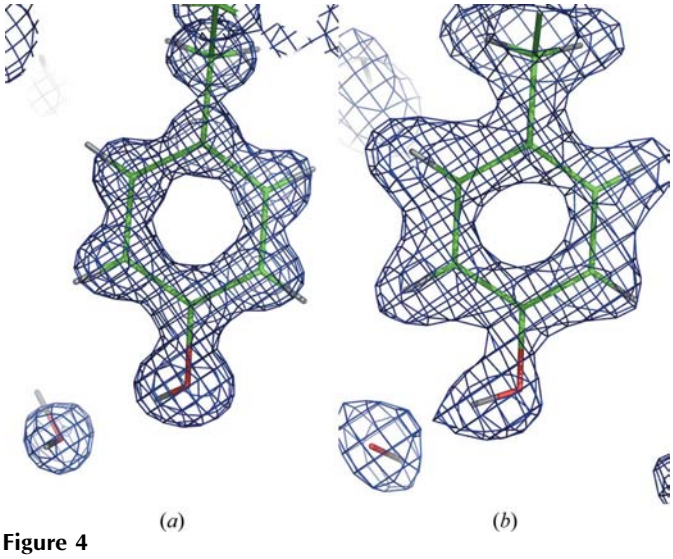


**Figure 4**
Electron and neutron sample maps at Tyr10. Simulated-annealing composite D-OMIT map density at 1.5$\sigma$ for D-rubredoxin computed from (*a*) an X-ray data set from at 100 K and (*b*) a neutron data set at 295 K. The increased visibility of the D atoms in the nuclear density map is striking.

$R_{work}$ = 18.7% and $R_{free}$ = 20.2%. Owing to the 1.1 Å resolution of the RT HD-rubredoxin X-ray data set, many of the main-chain atoms were modelled with anisotropic thermal parameters. 42 D atoms of water molecules were explicitly assigned when nuclear $F_o - F_c$ map density made their positions clear. Of the 37 heavy-water molecules refined in this structure, 14 were ultimately assigned as full $D_2O$ molecules with 'boomerang' nuclear density, a further 14 had 'stick' density for the O and one D atom and the remaining nine waters displayed only spherical nuclear density.

### 2.7. Computation of maps

The selection of a protocol for map computation was important in order to make a fair comparison between X-ray and neutron diffraction and to ensure unbiased maps. The purpose of computing a simulated-annealing composite-OMIT map (in which the atoms in a particular region of the map are omitted and the rest of the model is refined before computing the density for that region) is to remove model bias, usually in the early stages of structure rebuilding. Phasing power for atoms is strongest for the atoms nearby; considering protein structure rebuilding at the termini of a model, the map density near known atom positions is clearer than the density further away. Therefore, H atoms may more easily be visualized in difference maps than in composite-OMIT maps computed from X-ray data. However, simple H-OMIT or D-OMIT annealed difference maps are not comparable between neutron and X-ray maps, owing to H atoms (whether protium or deuterium) providing approximately half the scattering for a protein neutron diffraction experiment. To ensure true comparability of visualization, simulated-annealing composite deuterium-OMIT maps were computed with *nCNS via* the composite_omit_map_select.inp instruction file (kindly provided by Marat Mustyakimov); $\sigma_A$-weighted Fourier coefficients were used in the $2F_o - F_c$ map computation. This permitted the computation of simulated-annealing composite D-OMIT maps in which not more than 5% of the D atoms are omitted at a time. For X-ray structures, this process gave results comparable to simulated-annealing D-OMIT maps (comparison not shown). Sample electron-density maps from the region of Tyr10 of HD-rubredoxin are shown in Fig. 3 and a sample electron-density and nuclear density maps from D-rubredoxin are shown in Fig. 4. To compensate for the different refinement protocols used for different structures, *CNS* (Brünger *et al.*, 1998) and *nCNS* (Adams *et al.*, 2009) were used for overall *B*-factor scaling.

### 2.8. Analysis of peak heights

We measured the nuclear or electron density present in the simulated-annealing composite D-OMIT maps at each peptide D-atom position in each protein crystal structure. This was accomplished by treating the $P2_12_12_1$ map factors and phases (output by *nCNS*) with *SFTOOLS* (B. Hazes, unpublished program) to obtain a *P*1-expanded set of map structure factors and phases, as is required for analysis with *HYDENS* (B. Hazes, unpublished program). $\sigma$-Normalized electron-density and nuclear density peak heights at all individual atom positions were then computed with *HYDENS*. By means of a shell script, the *B* factors for the heavy atom bound to each D atom were tabulated with the peak height at each D atom.

## 3. Results and discussion

### 3.1. Refinement and analysis considerations

The goal of this work is to compare the visibility of D atoms in electron-density maps (from X-ray data sets) to that of D atoms in nuclear density maps (from neutron data sets). While the refined coordinates and ADPs of these rubredoxin crystal structures are all very similar, there were a number of modelling differences during refinement that played a role in determining the protocol for this analysis. While D-atom positions were refined individually in the joint XN refinements, all of the D-atom positions in the X-ray-only refinements were allowed to ride in chemically determined positions. These D atoms, whose positions can be described as chemically predetermined, formed the basis for the analysis that is the focus of this work. The positions of one or both D atoms could be assigned with varying levels of confidence from the nuclear density maps for many molecules of heavy water. As this introduced an additional level of subjectivity, however, we omitted the water atoms from the overall results of the analysis. Furthermore, the H atoms in the HD-rubredoxin structure were included in some plots to illustrate the sensitivity of the technique, but they were omitted from visibility comparisons.

We note that models of thermal motion may have some impact on the analysis. The high resolution of the X-ray data sets permitted the anisotropic refinement of many atoms, particularly in the main chain of the protein. However, the capability to compute maps from anisotropic atoms has not yet been implemented in *CNS* and *nCNS*, so all maps for this study were calculated from isotropic atoms. This implies that the electron-density maps used in this analysis may not reach the full potential of the data and model.

### 3.2. D atoms are eightfold more prominent in neutron maps

Analyzing the simulated-annealing composite D-OMIT maps from the X-ray and neutron data, we measured the nuclear or electron density present at each D-atom position in each protein crystal structure. For each D atom we correlated this value (measured in $\sigma$ level) to the thermal motion of the heavy (C, N or O) atom to which the D atom was bound. Figs. 5(*a*) and 5(*b*) show the detailed results of these calculations. As can be seen from these figures, even at relatively high $B$ factors of 30 Å$^2$ at least 50% of the D atoms remain visible at or above the 1$\sigma$ level in the neutron maps. Even at very low $B$ factors the X-ray data cannot provide this level of confidence for D-atom positions. Furthermore, the X-ray signal decays with increasing $B$ factor.

It is also enlightening to reduce these results to a simpler form: the average $\sigma$ level for D atoms in each structure or the fraction of 'visible' D atoms (those with peaks at a level of 1$\sigma$ or greater in the simulated-annealing composite D-OMIT map). For the 100 K 1.1 Å resolution X-ray-only refinements the average $\sigma$ levels at D-atom positions in the electron-density maps were 0.33 for D-rubredoxin and 0.23 for HD-rubredoxin. For the HD-rubredoxin RT X-ray only refinement this value is 0.27. However, in the nuclear density maps from joint XN refinement at RT the average $\sigma$ levels at D-atom positions were 2.4 for D-rubredoxin and 1.79 for HD-rubredoxin. We may thus compute the ratio $N_D/X_D$, where $N_D$ is the average peak height for D atoms in a neutron map ($\sigma$ units) and $X_D$ is the average peak height for D atoms in an X-ray map ($\sigma$ units). Computing this ratio, the mean signal at D-atom positions is eight times higher in each 1.7 Å resolution RT nuclear density map than in the corresponding 1.1 Å resolution 100 K electron-density map. Contrast this with the ratios for C ($N_C/X_C = 0.5$), N ($N_N/X_N = 0.6$), O ($N_O/X_O = 0.2$), S ($N_S/X_S = 0.03$) and Fe ($N_{Fe}/X_{Fe} = 0.1$). Therefore, although O and D have similar nuclear scattering lengths, X-ray diffraction provides a large relative advantage for O visualization. Thus, as expected, X-ray diffraction is superior for locating heavy atoms but neutrons excel at locating D atoms.

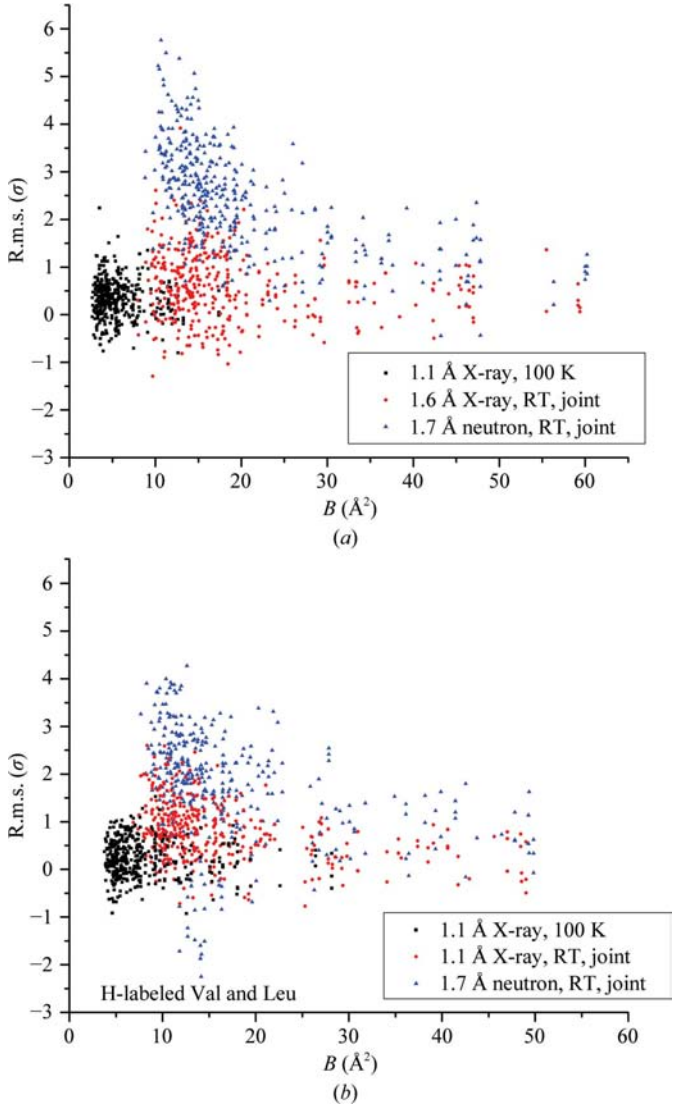


**Figure 5**
Peak-height level at each D-atom position *versus* the thermal motion ($B$ factor) for the bound heavy atom. (*a*) D-rubredoxin. (*b*) HD-rubredoxin. Although the Val and Leu methyl H atoms of HD-rubredoxin were not included in calculations, they are shown in this graph to display the sensitivity of the technique.

**Table 5**
Peak-visibility summary.

The mean $\sigma$ level for each atom type was computed in each simulated-annealing composite D-OMIT map. X, X-ray; N, neutron.

| | Z | HD, 100 K, X | HD, 295 K, X solo | HD, 295 K, X joint | HD, N joint | D, N joint | D, 295 K, X joint | D, 100 K, X |
|---|---|---|---|---|---|---|---|---|
| D (excluding DOD) | 1 | 0.22 | 0.27 | 0.78 | 1.79 | 2.4 | 0.6 | 0.32 |
| C | 6 | 5.2 | 4.4 | 3.1 | 2.7 | 3.0 | 2.4 | 5.5 |
| N | 7 | 7.3 | 6.0 | 4.2 | 3.8 | 4.7 | 4.1 | 7.2 |
| O (excluding DOD) | 8 | 7.5 | 5.6 | 4.3 | 1.4 | 2.0 | 4.6 | 7.5 |
| S | 16 | 24.7 | 21.2 | 13.0 | 0.8 | 0.6 | 12.5 | 23.6 |
| Fe | 26 | 45.7 | 40.5 | 24.5 | 4.6 | 4.3 | 22.1 | 43.7 |

**Table 6**
D-atom visibility summary.

| Composite D-OMIT cutoff ($\sigma$) | HD, 100 K, X | HD, 295 K, X solo | HD, 295 K, X joint | HD, N joint | D, N joint | D, 295 K, X joint | D, 100 K, X |
|---|---|---|---|---|---|---|---|
| Total | 388 | 388 | 365 (D only) | 365 | 378 | 378 | 388 |
| 0 | 276 | 277 | 326 | 350 | 372 | 300 | 311 |
| 1 | 8 | 20 | 125 | 291 | 342 | 110 | 19 |
| 1.5 | 1 | 1 | 49 | 234 | 294 | 43 | 3 |

Comparing the X-ray and neutron structures in terms of the overall fraction of visible D atoms presents an even more striking contrast. At the 1.5$\sigma$ level the joint XN structures determine 294/378 (78%) and 234/365 (64%) of all D atoms in the 1.7 Å resolution neutron maps for D-rubredoxin and HD-rubredoxin, respectively. At the 1.0$\sigma$ level this increases to 342/378 (90%) and 291/365 (80%) for D-rubredoxin and HD-rubredoxin, respectively. The X-ray-only 1.1 Å resolution 100 K structures determine only 3/388 of the D atoms in D-rubredoxin (0.8%) and only 1/388 (0.3%) of the D or H atoms in HD-rubredoxin at 1.5$\sigma$ electron density. At the 1.0$\sigma$ electon-density level this increases to 19/388 (5%) and 8/388 (2%) for D-rubredoxin and HD-rubredoxin, respectively. The values for the X-ray-only RT refinement of HD-rubredoxin are comparable to the 100 K values: the fractions above 1.5$\sigma$ and 1.0$\sigma$ are 1/388 (0.3%) and 20/388 (5%), respectively. These results are summarized in Tables 5 and 6.

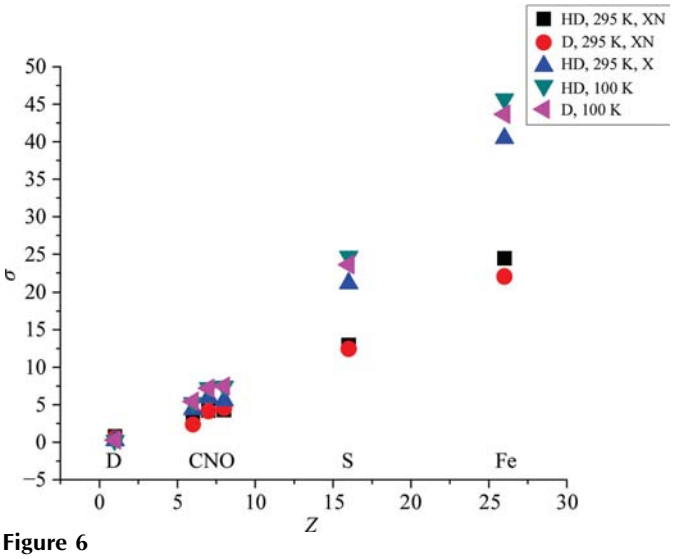


**Figure 6**
Average elemental peak height *versus* atomic number for electron-density maps computed from X-ray data.

**3.2.1. Some benefits of joint XN refinement**. Neutron refinements often suffer from a poor data-to-parameter ratio owing to the fact that there are approximately twice as many atoms to refine for a given protein. The inclusion of X-ray data in a neutron refinement offers a way to offset this problem in order to avoid local minima that may occur when using only medium-resolution neutron data (Wlodawer & Hendrickson, 1982) and can lead to better, clearer nuclear density maps than refinements against neutron data alone. The converse is also true, as the results of this study show. That is, the inclusion of neutron data in a refinement can improve the signal-to-noise level at D-atom positions in electron-density maps (relative to maps computed from X-ray-only refined structures). Specifically, the D-atom visibility in electron density is higher for crystal structures refined jointly with X-rays and neutrons: 43/378 (11%) of D atoms appear at or above 1.5$\sigma$ electron density for D-rubredoxin at 1.6 Å resolution and 49/365 (13%) for HD-rubredoxin at 1.1 Å resolution.

### 3.3. Counting electrons: C, N, O, S and Fe atoms can be differentiated on the basis of electron density

Crystallographic theory tells us that

$$\rho(x, y, z) = \frac{1}{V_c} \sum_{hkl=0}^{\infty} F(hkl) \exp[-i2\pi(hx + ky + lz)],$$

where $F(hkl) = \sum_{j=1}^{N} f_j \exp(i\varphi_j)$ and $f_{j,\theta(\theta\,=\,0)} = Z_j$ for X-ray scattering (Ladd & Palmer, 1985; $f \simeq -a_s$ for neutron scattering). Thus, we expect the electron density at an atom's position to depend on its atomic number $Z$ with a correction for thermal motion {the atomic scattering factor $B$-factor dependence for atom $j$ is $g_j = f_{j,\theta} T_{j,\theta}$, where $T_{j,\theta} = \exp[-B(\sin^2\theta/\lambda^2)]$} and we expect the nuclear density to depend on the coherent scattering cross-section (Table 7). The 1.1 Å resolution electron-density maps have sufficient detail to distinguish atom types by electron density. That is, the average electron-density level for each atom type varies almost linearly with atomic number in a given structure's map (Fig. 6). This is illustrated in Figs. 3(*a*), 3(*b*) and 4(*a*), in which the 1.5$\sigma$ contour for electron density at the hydroxyl position is visibly larger than that for the C atoms of the aromatic ring. The correlation becomes even closer to linear when a simplified multiplicative correction for $B$ factor is employed.

## 4. Conclusions

Single-crystal neutron diffraction has proved its strength in the analytical determination of hydrogen-bonding patterns,

**Table 7**
Atomic scattering for neutrons (Sears, 1992) and X-rays.

| Element | Neutron coherent scattering length (fm) | Atomic number ($Z$) |
|---|---|---|
| $^{1}$H | −3.7390 | 1 |
| $^{2}$H (D) | 6.671 | 1 |
| C | 6.646 | 6 |
| N | 9.36 | 7 |
| O | 5.803 | 8 |
| S | 2.847 | 16 |
| Fe | 9.45 | 26 |

water and hydroxyl orientations, and methyl rotor alignment. Neutrons can play an important role in structural biology. We have shown that 1.65 Å resolution neutron diffraction is eightfold more powerful for determining the positions of D atoms than 1.1 Å resolution X-ray diffraction, while X-ray diffraction remains more powerful for locating heavier atoms. We have also observed that D-atom visibility in electron-density and nuclear density maps correlates with atomic thermal motion, with more D atoms being visible in portions of the structure with lower $B$ values. While this effect is essentially linear in electron-density maps from X-ray structure refinements, even some structure regions of very high order do not have good D-atom visibility. Indeed, in the structures we have presented the expected mean electron density for a hypothetical D atom with $B = 0$ is only $\sim 0.5\sigma$. In contrast, D-atom visibility in nuclear density maps shows an exponential decay relative to increased $B$ factor. At the modest $B$ factor of 25 Å$^2$ the average D atom appears at $1.5\sigma$ in nuclear density maps of rubredoxin, demonstrating the power of neutron diffraction for direct location of D atoms.

We are grateful to Pavel Afonine (LBL) for assistance with *phenix.refine* enabling joint X/N refinement and to Marat Mustyakimov (LANL) for assistance with *nCNS* for computing X-ray and neutron simulated-annealing composite D-OMIT maps. We thank Bart Hazes (University of Alberta) for assistance with *SFTOOLS* and *HYDENS* and we thank Alberto Podjarny for helpful discussions about hydrogen visualization in various types of maps. This research at Oak Ridge National Laboratory's Center for Structural Molecular Biology (CSMB) was supported by the Office of Biological and Environmental Research using facilities supported by the US Department of Energy managed by UT-Battelle LLC under contract No. DE-AC05-00OR22725. This work was supported by an ORNL LDRD grant. We also thank SER-CAT and BioCARS-CAT at the APS for synchrotron beamtime, as well as the staff of the ILL in Grenoble, France for neutron beamtime and assistance with data collection. Data were collected on the Southeast Regional Collaborative Access Team (SER-CAT) 22-ID (or 22-BM) beamline at the Advanced Photon Source, Argonne National Laboratory. Supporting institutions may be found at http://www.ser-cat.org/members.html. Use of the Advanced Photon Source was supported by the US Department of Energy, Office of Science, Office of Basic Energy Sciences under Contract No. W-31-109-Eng-38. This research was supported in part by appointments to the DOE Science Undergraduate Laboratory Internships program and the ORNL Postdoctoral Research Associates Program at the Oak Ridge National Laboratory sponsored by the US Department of Energy and administered by the Oak Ridge Institute for Science and Education.

## References

Adams, P. D., Grosse-Kunstleve, R. W., Hung, L.-W., Ioerger, T. R., McCoy, A. J., Moriarty, N. W., Read, R. J., Sacchettini, J. C., Sauter, N. K. & Terwilliger, T. C. (2002). *Acta Cryst.* D**58**, 1948–1954.
Adams, P. D., Mustyakimov, M., Afonine, P. V. & Langan, P. (2009). *Acta Cryst.* D**65**, 567–573.
Arzt, S., Campbell, J. W., Harding, M. M., Hao, Q. & Helliwell, J. R. (1999). *J. Appl. Cryst.* **32**, 554–562.
Bau, R., Rees, D. C., Kurtz, D. M., Scott, R. A., Huang, H., Adams, M. W. W. & Eidsness, M. K. (1998). *J. Biol. Inorg. Chem.* **3**, 484–493.
Blakeley, M. (2009). *Crystallogr. Rev.* **15**, 157–218.
Blum, M. M., Mustyakimov, M., Ruterjans, H., Kehe, K., Schoenborn, B. P., Langan, P. & Chen, J. C. (2009). *Proc. Natl Acad. Sci. USA*, **106**, 713–718.
Brünger, A. T., Adams, P. D., Clore, G. M., DeLano, W. L., Gros, P., Grosse-Kunstleve, R. W., Jiang, J.-S., Kuszewski, J., Nilges, M., Pannu, N. S., Read, R. J., Rice, L. M., Simonson, T. & Warren, G. L. (1998). *Acta Cryst.* D**54**, 905–921.
Budayova-Spano, M., Fisher, S. Z., Dauvergne, M.-T., Agbandje-McKenna, M., Silverman, D. N., Myles, D. A. A. & McKenna, R. (2006). *Acta Cryst.* F**62**, 6–9.
Campbell, J. W., Hao, Q., Harding, M. M., Nguti, N. D. & Wilkinson, C. (1998). *J. Appl. Cryst.* **31**, 496–502.
Coates, L., Erskine, P. T., Wood, S. P., Myles, D. A. & Cooper, J. B. (2001). *Biochemistry*, **40**, 13149–13157.
Collaborative Computational Project, Number 4 (1994). *Acta Cryst.* D**50**, 760–763.
Dauter, Z., Lamzin, V. S. & Wilson, K. S. (1997). *Curr. Opin. Struct. Biol.* **7**, 681–688.
Di Costanzo, L., Moulin, M., Haertlein, M., Meilleur, F. & Christianson, D. W. (2007). *Arch. Biochem. Biophys.* **465**, 82–89.
Eidsness, M. K., Richie, K. A., Burden, A. E., Kurtz, D. M. Jr & Scott, R. A. (1997). *Biochemistry*, **36**, 10406–10413.
Emsley, P. & Cowtan, K. (2004). *Acta Cryst.* D**60**, 2126–2132.
Esposito, L., Vitagliano, L. & Mazzarella, L. (2002). *Protein Pept. Lett.* **9**, 95–106.
Evans, P. R. (1997). *Jnt CCP4/ESF–EACBM Newsl. Protein Crystallogr.* **33**, 22–24.
Gamble, T., Clauser, K. & Kossiakoff, A. (1994). *Biophys. Chem.* **53**, 15–25.
Garman, E. F. & Nave, C. (2009). *J. Synchrotron Rad.* **16**, 129–132.
Hakanpää, J., Linder, M., Popov, A., Schmidt, A. & Rouvinen, J. (2006). *Acta Cryst.* D**62**, 356–367.
Hazemann, I., Dauvergne, M. T., Blakeley, M. P., Meilleur, F., Haertlein, M., Van Dorsselaer, A., Mitschler, A., Myles, D. A. A. & Podjarny, A. (2005). *Acta Cryst.* D**61**, 1413–1417.
Holton, J. & Alber, T. (2004). *Proc. Natl Acad. Sci. USA*, **101**, 1537–1542.
Jenney, F. E. Jr & Adams, M. W. (2001). *Methods Enzymol.* **334**, 45–55.
Kossiakoff, A. A. (1983). *Annu. Rev. Biophys. Bioeng.* **12**, 159–182.
Kurihara, K., Tanaka, I., Chatake, T., Adams, M. W., Jenney, F. E. Jr, Moiseeva, N., Bau, R. & Niimura, N. (2004). *Proc. Natl Acad. Sci. USA*, **101**, 11215–11220.
Ladd, M. & Palmer, R. (1985). *Structure Determination by X-ray Crystallography*, 2nd ed. New York: Plenum.
La Placa, S. J. & Ibers, J. A. (1965). *Acta Cryst.* **18**, 511–519.
Leslie, A. G. W., Brick, P. & Wonacott, A. (1986). *Daresbury Lab. Inf. Q. Protein Crystallogr.* **18**, 33–39.

Liu, X., Hanson, B. L., Langan, P. & Viola, R. E. (2007). *Acta Cryst.* D**63**, 1000–1008.
Lovenberg, W. & Sobel, B. E. (1965). *Proc. Natl Acad. Sci. USA*, **54**, 193–199.
Meilleur, F., Contzen, J., Myles, D. A. & Jung, C. (2004). *Biochemistry*, **43**, 8744–8753.
Meilleur, F., Dauvergne, M.-T., Schlichting, I. & Myles, D. A. A. (2005). *Acta Cryst.* D**61**, 539–544.
Minasov, G., Wang, X. & Shoichet, B. K. (2002). *J. Am. Chem. Soc.* **124**, 5333–5340.
Murshudov, G. N., Vagin, A. A. & Dodson, E. J. (1997). *Acta Cryst.* D**53**, 240–255.
Ostermann, A., Tanaka, I., Engler, N., Niimura, N. & Parak, F. G. (2002). *Biophys. Chem.* **95**, 183–193.
Petrova, T. & Podjarny, A. (2004). *Rep. Prog. Phys.* **67**, 1565–1605.
Rosenbaum, G. *et al.* (2006). *J. Synchrotron Rad.* **13**, 30–45.
Schmidt, A. & Lamzin, V. S. (2002). *Curr. Opin. Struct. Biol.* **12**, 698–703.
Sears, V. F. (1992). *Neutron News*, **3**, 26–37.
Sheldrick, G. M. (2008). *Acta Cryst.* A**64**, 112–122.
Shu, F., Ramakrishnan, V. & Schoenborn, B. P. (2000). *Proc. Natl Acad. Sci. USA*, **97**, 3872–3877.
Vagin, A. & Teplyakov, A. (1997). *J. Appl. Cryst.* **30**, 1022–1025.
Weiss, K. L., Meilleur, F., Blakeley, M. P. & Myles, D. A. A. (2008). *Acta Cryst.* F**64**, 537–540.
Weiss, M. S. (2001). *J. Appl. Cryst.* **34**, 130–135.
Wlodawer, A. & Hendrickson, W. A. (1982). *Acta Cryst.* A**38**, 239–247.